Guiding synchrotron X-ray diffraction by multimodal video-rate protein crystal imaging

Justin A. Newman,[a] Shijie Zhang,[a] Shane Z. Sullivan,[a] Ximeng Y. Dow,[a] Michael Becker,[b] Michael J. Sheedlo,[a] Sergey Stepanov,[b] Mark S. Carlsen,[a] R. Michael Everly,[a] Chittaranjan Das,[a] Robert F. Fischetti[b] and Garth J. Simpson[a]*

[a]Department of Chemistry, Purdue University, 560 Oval Drive, West Lafayette, IN 47906, USA, and [b]GM/CA@APS, X-Ray Science Division, Argonne National Laboratory, Argonne, IL 60439, USA. *Correspondence e-mail: gsimpson@purdue.edu

Synchronous digitization, in which an optical sensor is probed synchronously with the firing of an ultrafast laser, was integrated into an optical imaging station for macromolecular crystal positioning prior to synchrotron X-ray diffraction. Using the synchronous digitization instrument, second-harmonic generation, two-photon-excited fluorescence and bright field by laser transmittance were all acquired simultaneously with perfect image registry at up to video-rate (15 frames s^{-1}). A simple change in the incident wavelength enabled simultaneous imaging by two-photon-excited ultraviolet fluorescence, one-photon-excited visible fluorescence and laser transmittance. Development of an analytical model for the signal-to-noise enhancement afforded by synchronous digitization suggests a 15.6-fold improvement over previous photon-counting techniques. This improvement in turn allowed acquisition on nearly an order of magnitude more pixels than the preceding generation of instrumentation and reductions of well over an order of magnitude in image acquisition times. These improvements have allowed detection of protein crystals on the order of 1 μm in thickness under cryogenic conditions in the beamline. These capabilities are well suited to support serial crystallography of crystals approaching 1 μm or less in dimension.

1. Introduction

X-ray free-electron lasers (XFELs) have recently paved a new way towards the determination of protein structures from <10 μm protein crystals through serial crystallography (Schlichting, 2015; Bogan, 2013; Chapman et al., 2011). Using the 'diffract-before-destroy' approach, a single-shot diffraction pattern is acquired from a single crystal prior to the crystal being destroyed. By rapidly probing multiple crystals, a full diffraction data set can be acquired. Serial crystallography is rapidly gaining traction due to the availability of high-fluence X-ray sources found at XFELs (Schlichting, 2015) and it is also beginning to be applied at synchrotron facilities (Stellato et al., 2014; Gati et al., 2014). Future planned upgrades to synchrotron facilities will soon allow for even brighter X-rays sources and allow for more rapid data collection (Borland, 2013).

As synchrotron facilities are moving towards fully automated crystal analysis and the target protein crystals are becoming increasingly smaller, a need is rapidly growing for reliable methods for automatically locating and centering protein crystals at synchrotron facilities (Aishima et al., 2010; Andrey et al., 2004; Cherezov et al., 2009; Moukhametzianov et al., 2008; Pothineni et al., 2006; Stepanov et al., 2011). Current
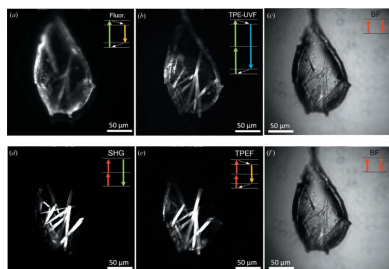
techniques employed for protein crystal detection include bright-field imaging (Andrey *et al.*, 2004; Jain & Stojanoff, 2007; Pothineni *et al.*, 2006), UV fluorescence imaging (Pohl *et al.*, 2004; Pothineni *et al.*, 2006; Vernede *et al.*, 2006) and X-ray rastering (Aishima *et al.*, 2010; Cherezov *et al.*, 2009; Hilgart *et al.*, 2011; Song *et al.*, 2007; Stepanov *et al.*, 2011). UV fluorescence imaging presents practical challenges with respect to background suppression, is not compatible with many of the most common loops and can induce photochemical damage (Pohl *et al.*, 2004; Pothineni *et al.*, 2006; Vernede *et al.*, 2006). Bright-field imaging has proven to be a reliable method for manual positioning when the crystals are large. However, as structure determination experiments are trending towards serial diffraction with small (~1 μm) crystals and automated centering, the relatively low contrast of bright-field imaging significantly reduces its utility for microcrystal and nanocrystal positioning. Furthermore, bright-field imaging methods generate contrast based on the transmission of light and thus become ineffective in highly turbid media such as the lipid cubic phase (LCP) used in the crystallization of integral membrane proteins. X-ray rastering, in which diffraction is used to identify position, is an attractive alternative (Aishima *et al.*, 2010; Cherezov *et al.*, 2009; Hilgart *et al.*, 2011; Song *et al.*, 2007; Stepanov *et al.*, 2011), but introduces X-ray exposure prior to diffraction analysis (Dettmar *et al.*, 2015). Furthermore, X-ray rastering is relatively time-consuming, requiring milliseconds to seconds per pixel for data acquisition corresponding to protein crystal centering times of several minutes (Aishima *et al.*, 2010). As detector technology advances, the time required for raster scanning continues to be reduced significantly (Broennimann *et al.*, 2006; Brönnimann *et al.*, 2001). However, diffraction from smaller crystals often requires raster scanning with higher fluxes and smaller beams for reliable background suppression to compensate for the loss in signal-to-noise ratio (SNR), exacerbating both issues of exposure and positioning time. In principle, the data collection can coincide with the diffraction raster scan, but in practice a sufficiently intense X-ray source can induce damage several micrometers from the position of exposure (Sanishvili *et al.*, 2011), such that alternative positioning methods that do not involve X-ray exposure are highly desirable.

Recently nonlinear optical (NLO) microscopy was integrated into a synchrotron beamline for on-line detection and centering of protein crystals (Madden *et al.*, 2013). The microscope provides both second-harmonic generation (SHG) and two-photon-excited UV fluorescence (TPE-UVF) imaging capabilities for detecting protein crystals. As complementary imaging techniques, SHG provides contrast from crystalline noncentrosymmetric material with no contributions from amorphous background (Kissick *et al.*, 2010*a*, 2011), and TPE-UVF provides sensitivity to tryptophan residues with minimal fluorescence signal outside the focal volume (Madden *et al.*, 2011). An estimated 84% of the protein crystals in the Protein Data Bank (PDB) are expected to be detectable by SHG (Haupert *et al.*, 2012), with TPE-UVF expected to increase this coverage. This instrument provides advantages over the existing methods due to the ability to image through turbid media with high SNR and without exposing the protein crystal to potentially damaging sources.

In an effort to offer further coverage of protein crystals, higher-resolution images and greater SNR, recent upgrades have been made and are described in the following paper. New imaging modalities have been included in the existing microscope to allow for three new imaging modalities, two-photon-excited fluorescence (TPEF) with 1064 nm excitation, single-photon fluorescence with 532 nm excitation and laser transmittance imaging, to complement the already existing suite of SHG and TPE-UVF. Also included is a discussion of the SNR enhancement afforded by upgrading the electronics to allow for synchronous digitization (Muir *et al.*, 2014).

2. Methods

Several new hardware modifications including changes to the optical path and upgrades to new data acquisition electronics have been made to the existing instrument for nonlinear optical guided synchrotron diffraction described previously (Madden *et al.*, 2013; Dettmar *et al.*, 2015). The new optical design upgrades center around providing additional imaging modes including laser transmittance imaging and single-photon fluorescence. Briefly, the multimodal imaging system utilizes a 1064 nm ultrafast laser (Fianium FemtoPower 1060, 50 MHz, 1060 fs pulses) to provide 1064 nm incident light at the sample for SHG, TPEF and bright-field imaging. A heated doubling crystal (Newlight Photonics Inc., SHG1663-IM, HTS 85141000) was used to frequency double the fundamental to provide 532 nm incident light at the sample for TPE-UVF and fluorescence imaging. The 1064 nm and 532 nm fundamental beams were scanned using a galvanometer driven mirror (Cambridge Technology, 6210 H) and a 7.8 kHz resonant scanning mirror (Cambridge Technology, 1-003-3002509). The fundamental was then focused on the sample by a 10× objective (Optem, 28-21-10). The signal generated at the sample was collected by a 25 mm lens (ThorLabs, f = 35 mm UV fused-silica). The fundamental 1064 nm light was then separated by a 700 nm long pass dichroic (Semrock, FF705-Di01-25×36) and detected with a photodiode (DET10A, Thorlabs). Bright-field images of the laser transmittance were generated from the photodiode signals. Another plano-convex lens (ThorLabs, f = 25.4 mm) coupled the SHG and fluorescence signals into a near-UV compatible liquid light guide (Oriel Instruments, 77554). Following recollimation with a plano-convex lens (ThorLabs, f = 25.4 mm) after exiting the light guide, both the SHG and TPE-UVF were then reflected off a primary dichroic beam splitter (Semrock, FF555-Di03-25×36), whereas the TPEF and single-photon fluorescence signals were transmitted and then focused onto the face of a photomultiplier tube (PMT) module (Hamamatsu, H10722-10) by a plano-convex lens (ThorLabs, f = 60 mm). The SHG and TPE-UVF signals were then separated at a second dichroic beam splitter (Chroma, z1064rdc-sp) for selective detection of SHG (through Chroma HQ530/30m and CVI 03FCG567/KG3 filters) and TPE-UVF (through Semrock,

SP01-532RS-25 and FF01-440/SP-25 filters). Both SHG and TPE-UVF signals were focused onto the faces of the PMT modules (Hamamatsu, H10722-10) by a plano-convex lens (ThorLabs, f = 60 mm). Full 512 × 512 pixel images are acquired with 0.25 µs pixel integration time resulting in a frame rate of 15 frames s^{-1}. Upgrades to the electronics and data acquisition cards (ATS9440, AlazarTech) have also been performed to allow for synchronous digitization. Synchronous digitization records the detector voltage only when the laser fires resulting in a significant reduction in non-time-coincident signal events. Further discussion of synchronous digitization can be found elsewhere (Muir *et al.*, 2014).

Full length mCherry was cloned into pGEX6P1 and transformed into Rosetta cells using standard cloning protocols. Cells were grown to an optical density of 0.4–0.6 and induced by the addition of 200 µ*M* IPTG, at which point the temperature was decreased to 18°C for 16–18 h. The cultures were harvested by centrifugation and lysed *via* French Press. Resulting lysates were then cleared by centrifuging at 100000*g* for 1 h and the protein was purified following standard GST purification protocols. The sample was further purified by size-exclusion chromatography and concentrated to a final concentration of 20 mg ml^{-1}. Protein crystals were grown using both sitting drop and hanging drop vapor diffusion

methods at room temperature following a previously published crystallization protocol (Shu *et al.*, 2006). Crystals appeared in drops within one to four days.

3. Results and discussion

Integration of synchronous digitization has allowed for simultaneous acquisition of SHG, TPEF and laser transmittance images in IR mode (1064 nm excitation) and simultaneous acquisition of TPE-UVF and fluorescence imaging in green mode (532 excitation). Fig. 1 demonstrates the multimodal imaging capabilities of the upgraded instrument for imaging mCherry crystals. The addition of new imaging modalities has provided complementary contrast mechanisms for detecting protein crystals. The original instrument used the complementary imaging modes of SHG, to provide selectivity for crystalline material, and TPE-UVF, for the detection of tryptophan residues. The addition of TPEF (IR mode) and fluorescence (green mode) provides a further contrast mechanism with sensitivity to color centers within the protein. TPEF is also shown to provide contrast from proteins that have been oxidized (Padayatti *et al.*, 2012). The optical sectioning capabilities of these NLO techniques allows for three-dimensional localization of the protein crystals within
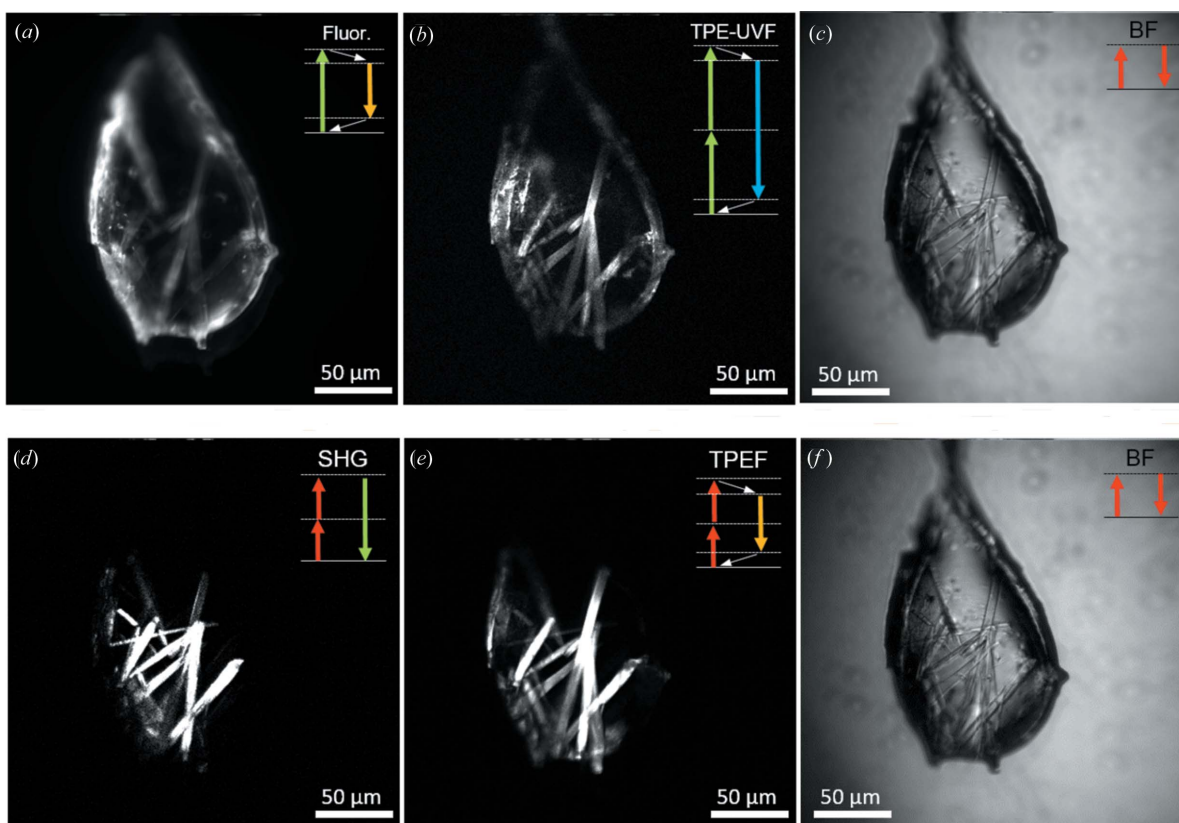
Figure 1
Multimodal images of mCherry crystals acquired at cryogenic temperature are shown. Images in the top row were acquired simultaneously using 532 nm incident light for one-photon-excited fluorescence in (*a*), two-photon-excited ultraviolet fluorescence in (*b*) and laser transmittance bright field of the residual 1064 nm light in (*c*). Images in the bottom row were acquired simultaneously using 1064 nm incident light for second-harmonic generation in (*d*), two-photon-excited visible fluorescence in (*e*) and laser transmittance bright field in (*f*). All images were acquired with a 0.25 µs pixel dwell time with 512 frames averaged together.

the sample mount. The video shown in the supporting information demonstrates the localization of protein crystals in three dimensions by acquiring ten images at 20 µm intervals through the depth of the sample. Whereas the axial resolution is noticeably worse than the spatial resolution, due to an ~20 µm depth of field, axial localization is still possible. More precise localization could be achieved by rotating the sample 90° and acquiring a z-stack of images through the sample.

Upgrading the data acquisition cards has allowed for full 512 × 512 images to be acquired, a significant improvement over the 256 × 128 images that were acquired using the previous data acquisition cards. The high-resolution images in combination with the SNR advantages of synchronous digitization (Muir et al., 2014) allow for detection of smaller crystals. Fig. 2 shows a zoomed-in portion of a full-frame image (given in the inset) demonstrating the ability to detect and resolve protein crystals with thicknesses of the order of ~1 µm under cryogenic conditions in the X-ray beam path. These small needles are challenging to discriminate based on the brightfield images, but are readily detectable in both the SHG and the TPEF imaging modalities.

Arguably the greatest benefit to upgrading the data acquisition cards to enable synchronous digitization is the improvement in the SNR of the images and the corresponding reduction in measurement time. The previous data acquisition cards were based on photon counting using electronic discrimination (i.e. a count was recorded each time a voltage transient crossed a preset threshold). This approach imposed two significant limitations. First, significant background contributions arose from photons generated by stray room light (i.e. LED screens on electronic components) striking the PMT as well as inherent dark-counts from spontaneous electron ejection from the photocathode. Second, the measurements were restricted to low light levels due to saturation. In synchronous digitization the laser is used as a master clock driving digitization of detector events that are time coincident with the clock. As a result, background from non-coincident detector events is largely suppressed. When the voltage transient is fast relative to the laser repetition rate as in the

present case (~1.5 ns and 20 ns, respectively), the improvements in noise rejection can be quite significant. Furthermore, the digital signals can be acquired and simultaneously processed both for low light levels by photon counting and for high light levels by recording the analog voltage (Kissick et al., 2010b).

In principle, the expected enhancement in the SNR for synchronous digitization can be predicted from statistics. The peak voltage generated by the detector is determined by a combination of two random events. First, the number of photons arriving at the detector for a given laser pulse is a Poisson-distributed random variable dependent on the mean for that position. Second, the voltage peak height distribution of the transient generated by each detected photon is also a random variable, as the gain varies stochastically for each photoelectron produced at the photocathode. If the probability of generating multiple photons at each laser pulse is low, the voltage peak height distribution represents the inherent distribution of the detector gain following ejection of an electron from the photocathode. Because gain is the product of multiple random events, the peak height distribution is described well by a lognormal probability density function.

In the case of asynchronous digitization, in which the digitization time is random relative to the photon arrival time, a third random variable is introduced into the mix as illustrated in Fig. 3. With the ultrafast pulsed laser, the rise and fall time for the voltage transient is non-negligible. An analytical model of the impulse response function (IRF) for the detector used in the instrument has been developed previously (Dow et al., 2015), as shown in equation (1), consisting of an exponential decaying component with some ringing:

$$IRF(\tau) = \exp\left(\frac{-\tau}{2.1}\right)\cos\left[\left(2\pi\frac{\tau}{5.4}\right) + 4.6\right], \quad \tau > 0. \quad (1)$$
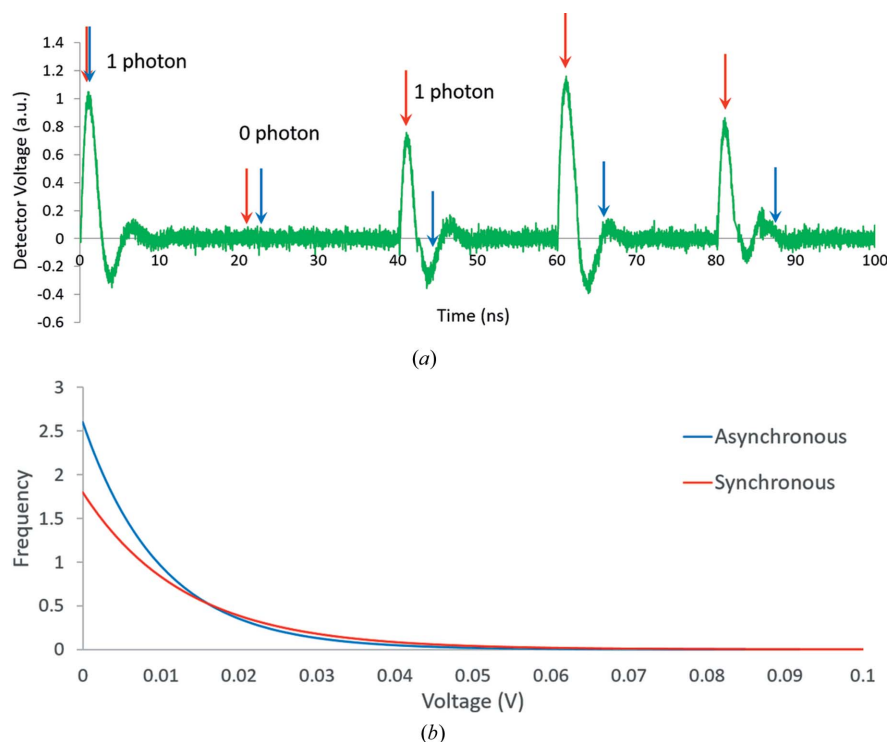
With synchronous digitization, each temporally coincident detector event can be optimized to overlap with the maximum position of the IRF. The recovered peak height distribution represents the inherent voltage distribution of the detector
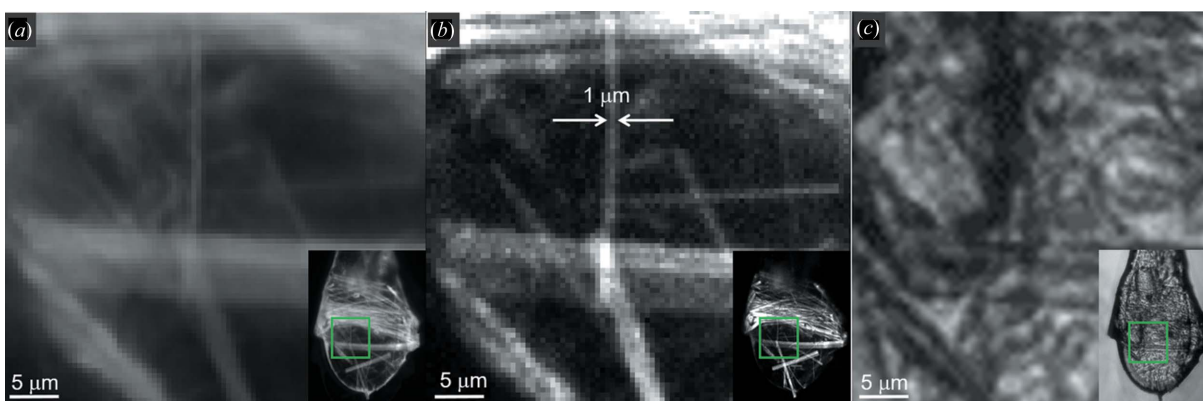
Figure 2
Zoomed-in regions are shown for different imaging modalities obtained simultaneously with 1064 nm incident light, with the expanded views provided in the insets: (a) two-photon-excited fluorescence, (b) SHG and (c) laser transmittance bright field. The two facing arrows highlight a crystalline needle with a cross-sectional diameter of ~1 µm. All images were acquired with 0.25 µs pixel dwell time with 256 frames averaged together.

(Fig. 3a). In contrast, the digitization events recorded with asynchronous digitization are spread out across the IRF, producing a broadening and lowering in the recovered peak height distribution (Fig. 3b). Analytical and numerical simulations of the peak height distributions observed by the detector using both synchronous digitization and asynchronous digitization were investigated to quantify the enhancement in SNR. Z-cut quartz was used to controllably generate SHG. The voltage peak height distributions for both synchronous digitization and asynchronous digitization were constructed by building the histograms of the observed voltages. A global threshold (determined by the background voltage of the detector) was applied to both peak height distributions to perform photon counting. The signal distributions were then fit to exponential decays (as a simplified model for a lognormal distribution), in which the decay constant ν effectively describes the width of the peak height distributions.

In order to assess the utility of the measurements acquired in this manner, simulations of the peak height distribution anticipated in asynchronous digitization were performed using the measured detector characteristics from the synchronous

Table 1
Exponential fit parameters for synchronous and asynchronous peak height distributions.

Parameters in the table were obtained from a fit of the measured distribution in voltages corresponding to photon events to the equation PHD(V) = $A \exp(-V/\nu)$. Uncertainties represent one standard deviation using the error derived from the fit.

	A	ν
Experimental synchronous fit	1.8 ± 0.6	0.013 ± 0.004
Experimental asynchronous fit	2.6 ± 0.6	0.010 ± 0.001
Predicted asynchronous fit	2.6 ± 0.3	0.0099 ± 0.0006

digitization data and the measured IRF. A comparison of the broadened peak height distribution observed in asynchronous digitization and the anticipated results generated from the synchronous digitization measurements is summarized in Table 1 and Fig. 3(b). The model first simulates the unbroadened signal voltage following the exponential decay observed in synchronous digitization, then multiplies each digitization event with a random location on the IRF. The same global threshold was applied to the resulting products and the histogram of the simulated signal was fit to an exponential decay.

The fit to the peak height distribution of the simulated signal in Table 1 is in excellent agreement with the fit to the peak height distribution of the experimentally acquired asynchronous acquisition. The accurate recovery of ν suggests that the IRF is the dominant source of SNR disparity between synchronous and asynchronous digitization, consistent with our hypothesis. The SNR enhancement afforded by synchronous digitization can be quantitatively estimated by comparing the integral of the IRF distribution for asynchronous digitization and a uniform distribution for synchronous digitization. The resulting integrals of the two distributions suggest an approximate 15.6-fold increase in SNR when using synchronous digitization over asynchronous digitization. The increase in SNR suggests significant reductions in measurement times for protein crystal detection. As a result, increases in both the frame rate (up to 15 Hz) and the image resolution can be realised for centering protein crystals on the beamline without significant loss in SNR.

The ability to detect protein crystals of ~1 µm allows for the use of NLO microscopy to guide serial crystallography diffraction analysis. By using the NLO microscope to rapidly image a sample, a list of coordinates for the location of many crystallites within the focal volume can be

Figure 3
Illustration of the SNR advantages afforded by synchronous digitization for low light detection, in which the digitizer is clocked to record the voltage of transients produced by single photons arriving synchronously with the firing of the laser. In the simulation of the raw time-dependent signal streaming from a detector in (a), transient signals are captured at the point of maximum signal-to-noise in synchronous digitization (red arrows). In contrast, asynchronous digitization (blue arrows) at low acquisition rates can miss single-photon events and underestimate photon count rates. Because the current produced from a single-photon absorption event is a random variable, the probability of obtaining a particular peak voltage is described by the peak height distribution, modeled herein by an exponential probability density function. Performing asynchronous digitization as in blue arrows in (a) results in a higher probability of detecting low-voltage transients illustrated in (b), with corresponding reductions in the recovered SNR.

generated and individually probed by the synchrotron. Only probing locations that are SHG-active can significantly reduce both the overall time of the diffraction analysis and the exposure to X-rays prior to data collection (*e.g.* by raster scanning of the X-ray beam).

As introduced previously, synchronous digitization allows for the acquisition of multiple channels spanning a broad dynamic range of signal levels from photon counting to signal averaging (Kissick *et al.*, 2013; Muir *et al.*, 2014). As such, high signal level imaging modalities, such as fluorescence and laser transmittance, can be integrated into a single platform along with low signal level imaging modalities (*i.e.* SHG, TPEF, TPE-UVF). Simultaneous acquisition of complementary imaging techniques provides a lower false negative rate resulting in more crystals being probed by the synchrotron.

Arguably the most important addition to the imaging suite is that of laser transmittance imaging. Because SHG is only sensitive to crystalline materials, the images often do not provide useful fiducials for overlaying the SHG image with conventional bright-field images. With the addition of the new data acquisition cards and the simultaneous acquisition of the complementary imaging modes (including laser transmittance), high-fidelity image overlay between the different images is achieved for all imaging modalities using the same incident wavelength (*i.e.* SHG, TPEF and bright field for IR mode, and TPE-UVF, fluorescence and bright field for green mode). Regions producing signal can be correlated to the laser transmittance images, which in turn provide the fiducials necessary for image correlation with existing bright-field architectures and centering algorithms employed by synchrotron facilities. It is important to note that a small spatial offset in the image plane is observed when comparing images acquired using green mode and IR mode. This small offset is a result of different reflective surfaces on one of the dichroic mirrors prior to the sample. Similarly, IR mode and green mode focus to different focal planes due to chromatic aberrations from focusing 532 nm light and 1064 nm light through the same objective.

The perfect image registry between the different simultaneous imaging modalities within a single-incident laser mode (*i.e.* green mode or IR mode) has the potential to be particularly beneficial in subsequent efforts to integrate algorithms such as machine learning to aid in automated crystal positioning. The bright-field images exhibit high spatial resolution but low contrast and sensitivity for crystals. In contrast, the SHG, TPE-UVF and TPEF provide high selectivity and tight confinement of position in three dimensions, but relatively low signal-to-noise. Finally, in the presence of a fluorophore with visible emission, the one-photon visible fluorescence provides high-signal-to-noise, but low spatial resolution, particularly along the optical axis. As a result, each of the individual measurements provides complementary information on crystal position, such that algorithms combining data from multiple orthogonal modalities are more likely to reliably identify crystal positions across broad classes of samples. However, combined analyses such as these are often frustrated by uncertainties in positional overlap between multiple modalities. The ability to acquire multimodal images concurrently in the current platform removes this ambiguity and facilitates automation for crystal centering.

4. Conclusions

Modifications to the on-axis NLO microscope for guided synchrotron diffraction have added three new image contrast mechanisms (TPEF, fluorescence and laser transmittance) to further complement SHG and TPE-UVF to reduce false negatives for protein crystal detection and centering on a synchrotron beamline. The new electronics now allow for full 512×512 simultaneous multimodal imaging with perfect overlay between the different imaging modalities using the same incident laser wavelength. The electronics upgrade to synchronous digitization has also allowed for a $\sim$16-fold increase in SNR. The increase in SNR directly contributes to the reduction in image acquisition times. Given the square-root dependence of SNR on integration time, the use of synchronous digitization corresponds to a $\sim$250-fold reduction in the required measurement time for comparable per-pixel SNR. The ability to visualize protein crystals at video rate using nonlinear optical methods (SHG, TPEF, TPE-UVF) further paves the way for practical high-throughput automated serial crystallography of protein microcrystals and nanocrystals.

References

Aishima, J., Owen, R. L., Axford, D., Shepherd, E., Winter, G., Levik, K., Gibbons, P., Ashton, A. & Evans, G. (2010). *Acta Cryst.* D**66**, 1032–1035.

Andrey, P., Lavault, B., Cipriani, F. & Maurin, Y. (2004). *J. Appl. Cryst.* **37**, 265–269.

Bogan, M. J. (2013). *Anal. Chem.* **85**, 3464–3471.

Borland, M. (2013). *J. Phys. Conf. Ser.* **425**, 042016.

Broennimann, Ch., Eikenberry, E. F., Henrich, B., Horisberger, R., Huelsen, G., Pohl, E., Schmitt, B., Schulze-Briese, C., Suzuki, M., Tomizaki, T., Toyokawa, H. & Wagner, A. (2006). *J. Synchrotron Rad.* **13**, 120–130.

Brönnimann, C., Baur, R., Eikenberry, E. F., Kohout, S., Lindner, M., Schmitt, B. & Horisberger, R. (2001). *Nucl. Instrum. Methods Phys. Res. A*, **465**, 235–239.

Chapman, H. N. *et al.* (2011). *Nature (London)*, **470**, 73–77.

Cherezov, V., Hanson, M. A., Griffith, M. T., Hilgart, M. C., Sanishvili, R., Nagarajan, V., Stepanov, S., Fischetti, R. F., Kuhn, P. & Stevens, R. C. (2009). *J. R. Soc. Interface*, **6**, S587–S597.

Dettmar, C. M., Newman, J. A., Toth, S. J., Becker, M., Fischetti, R. F. & Simpson, G. J. (2015). *Proc. Natl Acad. Sci. USA*, **112**, 696–701.

Dow, X. Y., Sullivan, S. Z., Muir, R. D. & Simpson, G. J. (2015). *Opt. Lett.* **40**, 3296–3299.

Gati, C., Bourenkov, G., Klinge, M., Rehders, D., Stellato, F., Oberthür, D., Yefanov, O., Sommer, B. P., Mogk, S., Duszenko, M., Betzel, C., Schneider, T. R., Chapman, H. N. & Redecke, L. (2014). *IUCrJ*, **1**, 87–94.

Haupert, L. M., DeWalt, E. L. & Simpson, G. J. (2012). *Acta Cryst.* D**68**, 1513–1521.

Hilgart, M. C., Sanishvili, R., Ogata, C. M., Becker, M., Venugopalan, N., Stepanov, S., Makarov, O., Smith, J. L. & Fischetti, R. F. (2011). *J. Synchrotron Rad.* **18**, 717–722.

Jain, A. & Stojanoff, V. (2007). *J. Synchrotron Rad.* **14**, 355–360.

Kissick, D. J., Gualtieri, E. J., Simpson, G. J. & Cherezov, V. (2010*a*). *Anal. Chem.* **82**, 491–497.

Kissick, D. J., Muir, R. D. & Simpson, G. J. (2010*b*). *Anal. Chem.* **82**, 10129–10134.

Kissick, D. J., Muir, R. D., Sullivan, S. Z., Oglesbee, R. A. & Simpson, G. J. (2013). *Proc. SPIE*, **8657**, 86570E.

Kissick, D. J., Wanapun, D. & Simpson, G. J. (2011). *Annu. Rev. Anal. Chem.* **4**, 419–437.

Madden, J. T., DeWalt, E. L. & Simpson, G. J. (2011). *Acta Cryst.* D**67**, 839–846.

Madden, J. T. *et al.* (2013). *J. Synchrotron Rad.* **20**, 531–540.

Moukhametzianov, R., Burghammer, M., Edwards, P. C., Petitdemange, S., Popov, D., Fransen, M., McMullan, G., Schertler, G. F. X. & Riekel, C. (2008). *Acta Cryst.* D**64**, 158–166.

Muir, R. D., Sullivan, S. Z., Oglesbee, R. A. & Simpson, G. J. (2014). *Rev. Sci. Instrum.* **85**, 033703.

Padayatti, P., Palczewska, G., Sun, W., Palczewski, K. & Salom, D. (2012). *Biochemistry*, **51**, 1625–1637.

Pohl, E., Ristau, U., Gehrmann, T., Jahn, D., Robrahn, B., Malthan, D., Dobler, H. & Hermes, C. (2004). *J. Synchrotron Rad.* **11**, 372–377.

Pothineni, S. B., Strutz, T. & Lamzin, V. S. (2006). *Acta Cryst.* D**62**, 1358–1368.

Sanishvili, R., Yoder, D. W., Pothineni, S. B., Rosenbaum, G., Xu, S., Vogt, S., Stepanov, S., Makarov, O. A., Corcoran, S., Benn, R., Nagarajan, V., Smith, J. L. & Fischetti, R. F. (2011). *Proc. Natl Acad. Sci. USA*, **108**, 6127–6132.

Schlichting, I. (2015). *IUCrJ*, **2**, 246–255.

Shu, X., Shaner, N. C., Yarbrough, C. A., Tsien, R. Y. & Remington, S. J. (2006). *Biochemistry*, **45**, 9639–9647.

Song, J., Mathew, D., Jacob, S. A., Corbett, L., Moorhead, P. & Soltis, S. M. (2007). *J. Synchrotron Rad.* **14**, 191–195.

Stellato, F. *et al.* (2014). *IUCrJ*, **1**, 204–212.

Stepanov, S., Hilgart, M., Yoder, D. W., Makarov, O., Becker, M., Sanishvili, R., Ogata, C. M., Venugopalan, N., Aragão, D., Caffrey, M., Smith, J. L. & Fischetti, R. F. (2011). *J. Appl. Cryst.* **44**, 772–778.

Vernede, X., Lavault, B., Ohana, J., Nurizzo, D., Joly, J., Jacquamet, L., Felisaz, F., Cipriani, F. & Bourgeois, D. (2006). *Acta Cryst.* D**62**, 253–261.